

International Conference on Space Optics—ICSO 2022

Dubrovnik, Croatia

3–7 October 2022

Edited by Kyriaki Minoglou, Nikos Karafolas, and Bruno Cugny,



Micro-integrated optical systems and qualification of adhesive integration technologies for cold atomic quantum sensors



Micro-integrated optical systems and qualification of adhesive integration technologies for cold atomic quantum sensors

M. Christ^{a,b}, A. Stiekel^{a,b}, C. Stölmacker^a, C. Zimmermann^a, A. Kassner^c, M. Wurzc, and M. Krutzik^{a,b}

^aFerdinand-Braun-Institut (FBH), Gustav-Kirchhoff-Strasse 4, 12489 Berlin, Germany

^bHumboldt-Universität zu Berlin, Joint Lab Integrated Quantum Sensors, Newtonstraße 15, 12489 Berlin, Germany

^c Leibniz University Hanover, Institute of Micro Production Technology, An der Universität 2, 30823 Garbsen, Germany

ABSTRACT

Cold atom based quantum sensors require robust and miniaturized optical systems for applications on mobile platforms. A micro-integrated optical system (volume ~ 25 mL) for trapping and manipulation of neutral atoms is presented. This setup focuses and precisely overlaps two high power laser beams (1064 nm, up to 2 W total, $w_R = 34$ μm) launched via a single-mode, polarization maintaining optical fiber, thereby realizing a crossed beam optical dipole trap (ODT). Adhesive bonding is qualified in application relevant geometries and material systems of micro-integrated optical systems for application on mobile platforms or space. Fused silica test blocks (bond area 2×4 mm²) are bonded with four different adhesives on silicon wafers. These samples are aged by thermal cycling (up to -55 °C to 150 °C) and/or gamma-radiation (10 000 mSv) and subsequently the bond strength is evaluated by die shear testing according to MIL-STD-883L. The influence of the environmental aging on the bond strength is presented, the failure mode and the influence of fillets discussed. In addition, the effects of plasma cleaning on the bond strength in this geometry is presented.

Keywords: integrated quantum sensors, optical dipole trap, micro-integration, miniaturization, optical systems, adhesive bonding, environmental qualification, thermal cycling, radiation, plasma cleaning

1. MINIATURIZED OPTICAL SYSTEMS FOR QUANTUM SENSING

Due to their unrivalled accuracy and precision, atomic quantum sensors and clocks operated in field or space may improve on applications in the areas of navigation, timekeeping, exploration, and can be used to address fundamental questions of modern physics.¹ The transition from laboratory-based setups to field- and space-compatible devices requires a high degree of integration and miniaturization to fulfill requirements on size, weight, and power (SWaP) budgets. Moreover, a high environmental robustness must be achieved for operation on mobile platforms, i.e. with regard to mechanical and thermal loads and radiation hardness.

The physics package of a cold atomic quantum sensor consists of multiple key components, usually including atom source, ultrahigh vacuum system and the surrounding optics setup. In many cases an optical dipole trap (ODT)² is used for optical trapping and cooling of the atomic ensemble that can be realized by far detuned optical light fields tailored to the used species and foreseen application. Such an ODT relies on high light intensities and gradients, which are realized by focusing high power laser to narrow waists. A configuration to achieve strong spatial confinement of the atoms in all three dimensions is a crossed beam ODT, where two high-power laser beams are tightly focused and precisely overlapped at a specific angle. This requires laser light to be guided around the cold atom setup with mirrors, beam-splitters, waveplates, polarizers and subsequently focused and overlapped inside the ultra-high vacuum chamber. Although such a large-aperture setup yields very small optical waists and thus large trap depths, it requires frequent re-alignment, is sensitive to thermal fluctuations or mechanical disturbances and occupies a rather large volume (about 2 to 3 L). While being feasible for lab-based setups, another approach is necessary for mobile setups on earth or microgravity platforms.

Corresponding author: Marc Christ, marc.christ@fbh-berlin.de, www.fbh-berlin.de

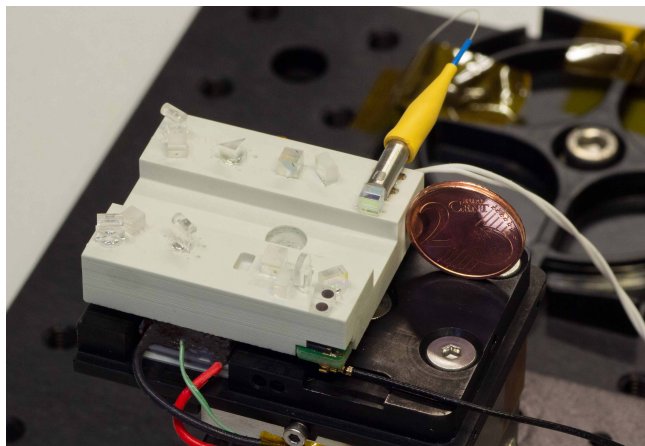


Figure 1. Miniaturized optical system to be used in a cold atom-based quantum sensor. Two beams (1064 nm, 1 W each) with overlapping focus ($w_R = 34\ \mu\text{m}$) create a so-called optical dipole trap, which can be used for trapping, cooling and manipulating rubidium atoms.

Within our work at the Ferdinand-Braun-Institut (FBH) we address the miniaturization and integration of the quantum sensor's physics package to small field and space compatible setups. Advanced micro-integration methods are established for the miniaturization of narrow linewidth diode lasers,³ proved their suitability in sounding rocket missions^{4–7} and will be used for the diode-based laser sources for the BECCAL mission aboard the ISS.⁸ These methods are adapted and used to realize a compact crossed beam optical dipole trap displayed in Fig. 1. The setup is operated at 1064 nm and injected by a light source via a single-mode, polarization-maintaining fiber and a collimator, generating a beam of 1 mm diameter on a ceramic bench. After the collimator, the light is polarized and split into two paths with perpendicular linear polarization. Both paths are focused to a waist radius of $w_R = 34\ \mu\text{m}$ and precisely overlapped. The center aperture of the optical system gives clearance for one of the beams of a magneto-optical trap (MOT), a first stage to trap and cool atoms. The overall optical system has a footprint of $36 \times 43\ \text{mm}^2$ and a volume of $\sim 25\ \text{mL}$ including optics. The optical setup can be operated with optical powers up to 2 W cw and exhibits an exceptional thermal and mechanical stability when operated at up to $60\ ^\circ\text{C}$ during tests. Currently the miniaturized crossed beam ODT is operated within a cold atom experiment. In summary, the micro-integration approach led to a substantial miniaturization of the optical system and simultaneously a high passive stability, both key factors for future applications on mobile and space-based platforms.

Based on this setup, we work on combining optical systems with an atom chip.⁹ The next generation of such chips is currently being developed at the Institute of Micro Production Technology (IMPT)¹⁰ and is based on silicon wafers with current conductor paths manufactured by micro-fabrication methods and mirror coatings. Such a chip allows to generate ultra-cold atom ensembles with high cycle times, enabled by steep magnetic fields with high trapping frequencies, forming, e.g., chip-based Ioffe-Pritchard traps. Ultimately, we aim to combine a micro-integrated optical setup with an atom chip within the ultra-high vacuum (UHV) environment of the physics package. This enables atom trapping configurations like purely optical or hybrid magneto-optical traps in the vicinity of the atom chip surface, while achieving a compact overall setup with high alignment stability. Such a setup requires miniaturized optical setups with high pointing stability and UHV compatibility. To assemble our optical systems, adhesive integration methods are used. They have the advantages of ease of application, short setup times, low cost and suitable mechanical and thermal properties. In our experience, they enable precise alignment of micro-optics, and the integration process is highly reproducible. The application of quantum sensors in field and space imposes further requirements on their e.g., mechanical, thermal, and radiative resilience.

2. MECHANICAL AND ENVIRONMENTAL QUALIFICATION OF ADHESIVES

To qualify the used adhesive integration methods for the desired applications, mechanical and environmental tests are conducted. The mechanical properties of an adhesive joint, i.e. bond strength, modulus, . . . , depend not

only on the used adhesive. The materials involved, their surface properties, cleaning, adhesive layer thickness and the curing procedure itself have a major influence on the formation of the adhesive's polymer network and thus the mechanical properties of the joint. In this study, test samples of adhesive joints with application-related geometries and materials are set up and environmentally aged by thermal cycling and radiation exposure. Subsequently their mechanical bond strength is characterized by shear strength tests.

2.1 Sample materials and setup

The investigated samples and setup procedures are described in Ref. 11 and summarized in the following. The samples consist of precision fused silica glass blocks with a footprint of $2 \times 4 \text{ mm}^2$, a typical bond area for our miniaturized optical systems. For the presented shear strength tests the glass bodies are cuboid. In the future, also tensile strength tests with trapezoidal sample bodies are planned. The lateral surfaces are polished to ensure reproducible UV light transmission for curing the adhesive. To ensure a reproducible bond area, the glass surface forming the bond is of very low roughness (surface profile height $R_t \leq 5 \text{ nm}$).

Simple silicon wafers are used as the substrate. Pre-tests with surface variations, e.g., by passivation or gold coating, showed similar behavior in terms of die shear strength and failure mode. For easy handling, the wafers are cut into $10 \times 10 \text{ mm}^2$ squares. The test samples are set up with different epoxy adhesive systems, cured according to the datasheets and their bond strength systematically investigated. The four different one or two component epoxy adhesives used, are common in optomechanics industry and have different curing mechanisms:

- **Adhesive 1 and 2:** purely UV curing epoxy adhesives.
- **Adhesive 3 and 4:** hybrid curing epoxy systems, thus after the UV-light cure to fix the component a subsequent thermal cure at $120 \text{ }^\circ\text{C}$ with a holding time of 30 min and a ramp of $10 \text{ }^\circ\text{C min}^{-1}$ for heating and cooling is used.

Fig. 2 shows the setup of the adhesive samples. Prior to assembly, all components are cleaned with isopropanol in an ultrasonic bath to remove contaminations e.g., by hydrocarbons and particles. Subsequently, the samples are wiped with acetone and a lint-free lens tissue, dried with dry nitrogen, inspected with a microscope and any remaining particles removed with a fiber optics cleaning swap. The glass test body is then attached to a micro-integration system to align it parallel to the substrate and to determine the zero-gap position. Next, the test body is lifted off the substrate and 240 nL of adhesive is applied with a pneumatic dispenser system which, after calibration for the specific adhesive under test, allows precise adhesive application down to 20 nL. By moving the test body back towards the substrate, the gap for the adhesive layer is set to $30 \text{ }\mu\text{m}$ and the applied adhesive is cured with UV light using an intensity-calibrated mercury light source. The UV-light is guided to the sample via two optical fiber light guides fixed at a defined distance in the sample holder, compare Fig. 2, in order to ensure reproducible exposure for curing of the adhesive layer.

2.2 Environmental aging and mechanical adhesive tests

The general requirements, the adhesive joints need to fulfill, are summarized in Ref. 11. Within this work, we specifically address influences of thermal and radiative stress on the shear strength of adhesive bonds. The selected test conditions follow the ESCC 23201, and the standards specified therein. Thermal cycling is performed at IMPT with a Vötsch VT3 7006 S2, which features one hot and one cold temperature chamber and thus quick cycling between temperatures. Radiative stress is applied by exposure to a cobalt-60 source at the Helmholtz Zentrum Berlin, emitting gamma rays at 1.17 MeV and 1.33 MeV. The adhesive samples are exposed to the following sets of different environmental conditions:

- **Ref:** Reference, no thermal or radiative stress applied.
- **TC A:** Thermal cycling according to MIL-STD-883L Test Method 1010.8 A: $-55 \text{ }^\circ\text{C}$ to $85 \text{ }^\circ\text{C}$, 100 cycles, dwell time 20 min, transfer time of 10 s between temperature chambers.
- **TC B:** Thermal cycling adapted from MIL-STD-883L Test Method 1010.8 B with an increased upper holding temperature: $-55 \text{ }^\circ\text{C}$ to $150 \text{ }^\circ\text{C}$, 100 cycles, dwell time 20 min, transfer time of 10 s between temperature chambers.

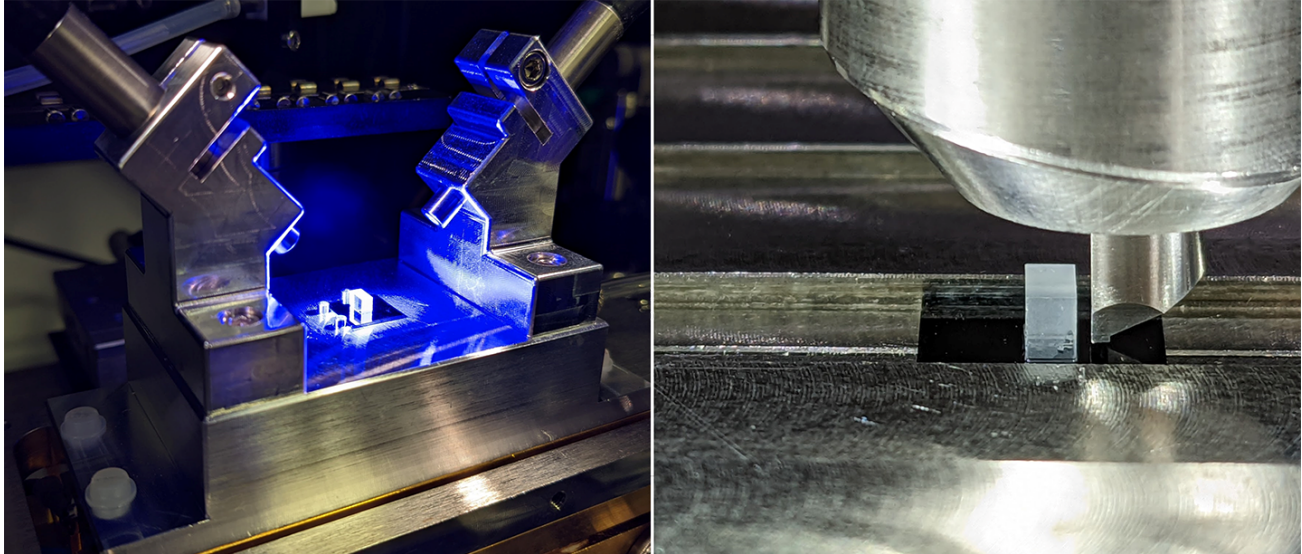


Figure 2. Left: sample holder with mount for UV-light guide and a glass test block during UV-cure, after alignment with a tweezer at the micro-integration facility. Right: adhesive sample in the bond tester with the shear tool approaching the glass test block.

- **Rad:** γ -radiation dose of 10 000 mSv
- **Rad & TC B:** Radiation exposure according to Rad and subsequent thermal cycling TC B.

For each test condition and each adhesive, one sample set, consisting of six samples, is prepared. Thus, in total 120 test samples are assembled. The mechanical bond strength of the adhesive joints is evaluated by destructive shear strength testing according to MIL-STD-883L Test Method 2019.9 'Die Shear Strength' with a bond tester (Nordson Dage 4000 Plus), compare Fig. 2, with an accuracy $\leq 1\%$ for the recorded force values. The results are displayed in Fig. 3 and compared to the required shear strength to fulfill MIL-STD-883L Test Method 2019.9 for an 8 mm^2 die of 24.5 N (factor 1.0x) or 49 N (factor 2.0x). Additionally, on the second y-axis the shear strength is scaled to g-force, assuming a weight of 0.044 g for the fused silica test body. In general, a scattering of the measurement results can be observed, although particular care was taken to keep the sample preparation, cleaning, and set-up procedure as comparable as possible for all samples. This can be caused by multiple reasons during the set-up or test procedure, e.g., residual contamination on the interface surfaces or microscopic variations of their structure, poor alignment precision of the samples, the adhesive pot life and thus variation of adhesive viscosity during sample preparation or human error when assembling and testing the samples. However, during set-up of our micro-optical systems we expect the same influences on the bonding process and thus the study yields representative results. Another error source might be the alignment of the die shear tool to the test body in the bond tester, which can lead to a deviation from the desired shear test geometry to a shear and torsion test geometry. The bond tester first aligns the shear tool automatically to the silicon substrate via touchdown. Subsequently the shear tool is aligned optically to the glass block with an expected accuracy of $\leq 1^\circ$. Additionally, a low force rotation joint on the machine corrects for small deviations once the shear tool touches the glass test body. Thus, we assume the error of the test method to be significantly smaller than the observed scattering of the shear test values. A detailed discussion of the of the results displayed in Fig. 3 follows at the end of this section.

The failure mechanism of an adhesive joint is categorized according to DIN EN ISO 10365, compare Ref. 12, as follows:

- **AF** adhesive fracture on one or both adherent's surfaces. Hence, the fracture occurred at the interface of adhesive and adherent.
- **CF** cohesive fracture within the adhesive layer.

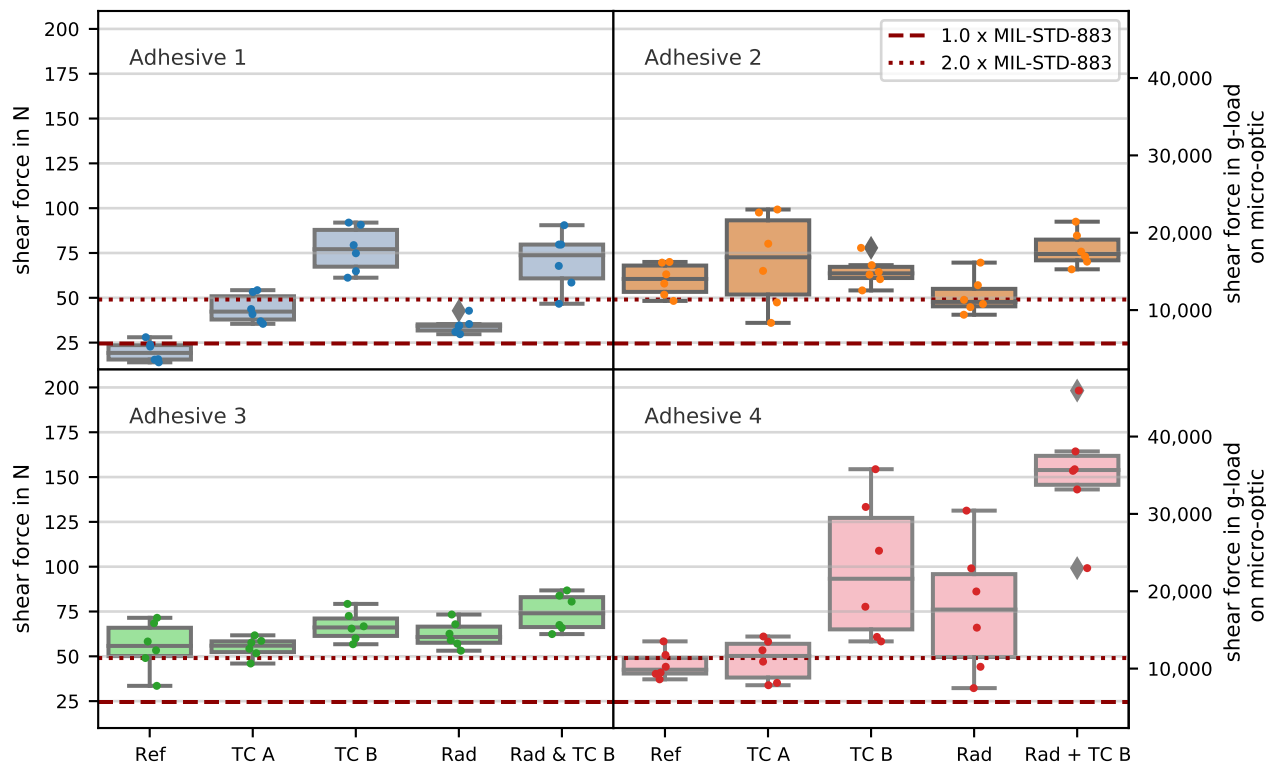


Figure 3. Mechanical bond strength of the tested adhesives evaluated by shear strength testing and displayed as boxplot. Outliers from the boxplot evaluation are displayed as grey diamond. In addition, the measurement points are plotted as an intuitive guide to the results.

- **SFS** special cohesive fracture close to the adherent's surfaces.
- **ACF** adhesive and cohesive fracture, a mixture of AF and CF.
- **JF** adherent fracture, either the fused silica block or the silicon substrate fractured.

Microscope images of substrate and glass block are recorded after shear strength test for every sample and categorized by their failure mechanism. Exemplary images for each failure mode are depicted in Fig. 4. The results of the shear strength measurements are assigned to the failure modes, as depicted in Fig. 5. Furthermore, the fracture images are evaluated whether the bond has a fillet of adhesive. This describes a partial adhesive joint at the lateral surfaces of the glass body formed by adhesive flowing out of the gap. Such a geometry is expected to increase the bond strength and influence the failure mode.^{13,14} If the image shows a fillet on at least three sides, the bond is categorized as 'with fillet' and marked accordingly in Fig. 5.

This evaluation gives valuable information for optimization of the adhesive bond. As shown, fracture modes vary for the chosen adhesives, the environmental stress and within each sample set. The highest bond strength is achieved by either **JF** or **CF** fracture modes, which is an expected behavior.¹⁵ In this case the bonding at the interface is stronger than the materials and either the adhesive layer (**CF**) or the Si wafer or the glass block (**JF**) fracture, but not the interfaces of the joint. As expected,¹³ these failure modes correlate very strongly with the occurrence of the fillet due to beneficial force application into the joint and less stress onto the interfaces of adhesive and adherents during die shear strength testing.

For the samples with the lowest bond strength the failure mode is **AF** or **ACF**, a complete or partial adhesion failure at one of the interfaces between adhesive and adherent. In this study, the failure occurred mostly at the

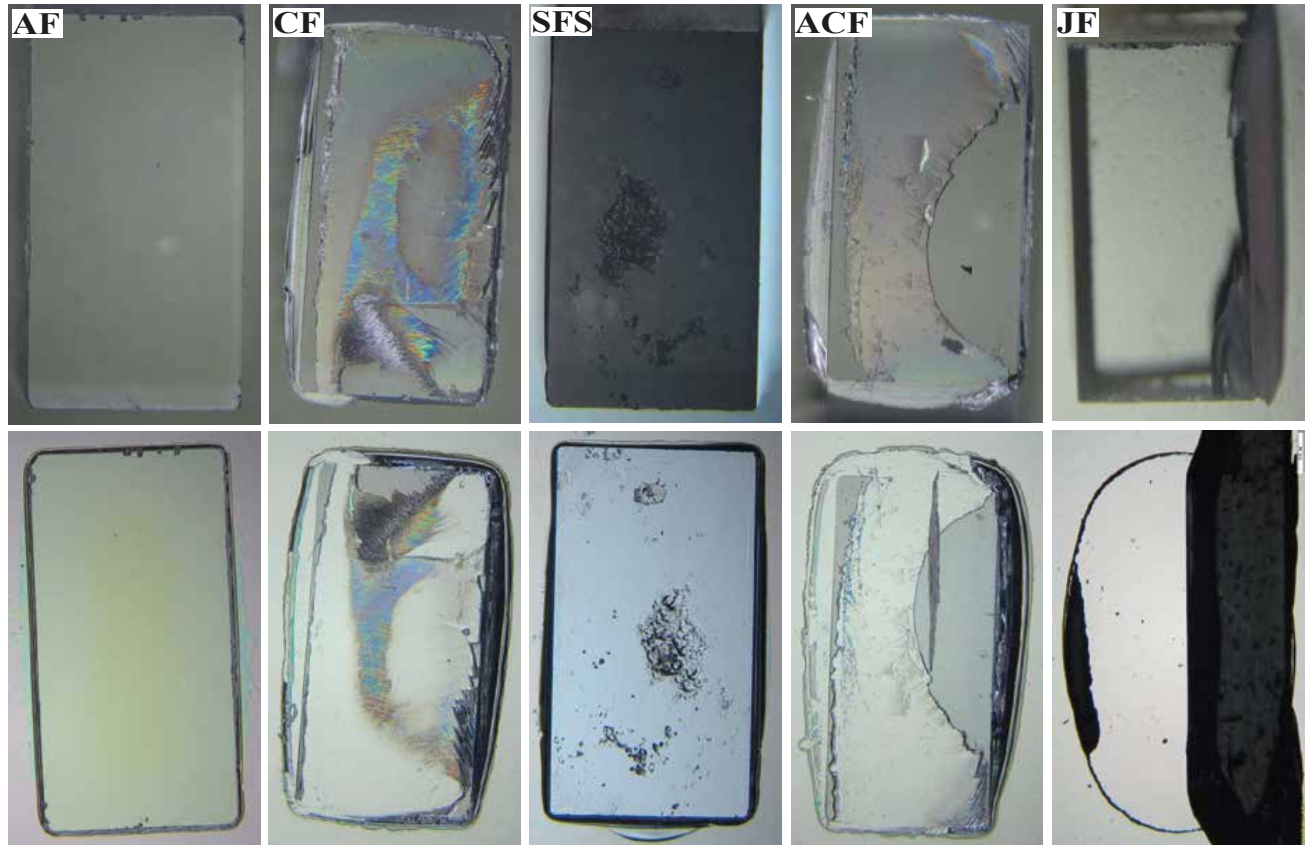


Figure 4. Exemplary microscope images for the different adhesive failure modes of glass block (upper) and substrate (lower), recorded after die shear strength test. The failure mode is categorized according to the fracture pattern and their characteristics explained in the text.

interface to the fused silica test body. This is due to insufficient bonding of the adhesive's polymer chains to the substrate and can be caused by contamination on the glass surface or insufficient wetting.

The presented shear strength dataset in Fig. 3 shows different influence of the environmental stresses, evaluated by die shear testing for four different adhesives. The fracture mode and the influence of the adhesive fillet is evaluated from microscope images of substrate and glass block and compiled in Fig. 5. Bond strength of **adhesive 1** increases with exposure to environmental stresses. The reference set does not pass the MIL-STD-883L Test Method 2019.9. Thermal aging according to TC A or TC B increases the bond strength of adhesive 1. This is also the case for radiation exposure Rad and a combination of both Rad + TC B. The sample set for Ref and Rad do not have fillets and exhibit AF and ACF failure modes. Hence these sets are not fully comparable to the other environmentally aged sample sets. However, the samples aged with TC A, TC B and Rad & TC B are comparable and the bond strength increases with these environmental stresses. This could indicate that, although this is a purely UV curing adhesive, the adhesive is not fully cured by the UV light and contains uncured monomers. The fast UV-cure of the adhesive could also lead to internal stresses in the polymer network. Application of external thermal or radiative energy increases the cross-linking of the polymer network and polymers can re-arrange, leading to a better cured adhesive layer with less internal stress.

The bond strength of the second purely UV curing type, **adhesive 2**, shows much less variation when exposed to thermal and radiative stresses and the bond strength increases after thermal exposure. The sample set for adhesive 2 shows comparable failure modes and occurrence of fillets for all assembled test samples. For this adhesive the bond strength exhibits a small decline when exposed to γ -radiation according to Rad compared to the reference set. This indicates that the cross-linking during UV cure leads to a high degree of cure, while the radiation exposure causes a partial destruction of the cross-linked polymer network and hence a reduced bond

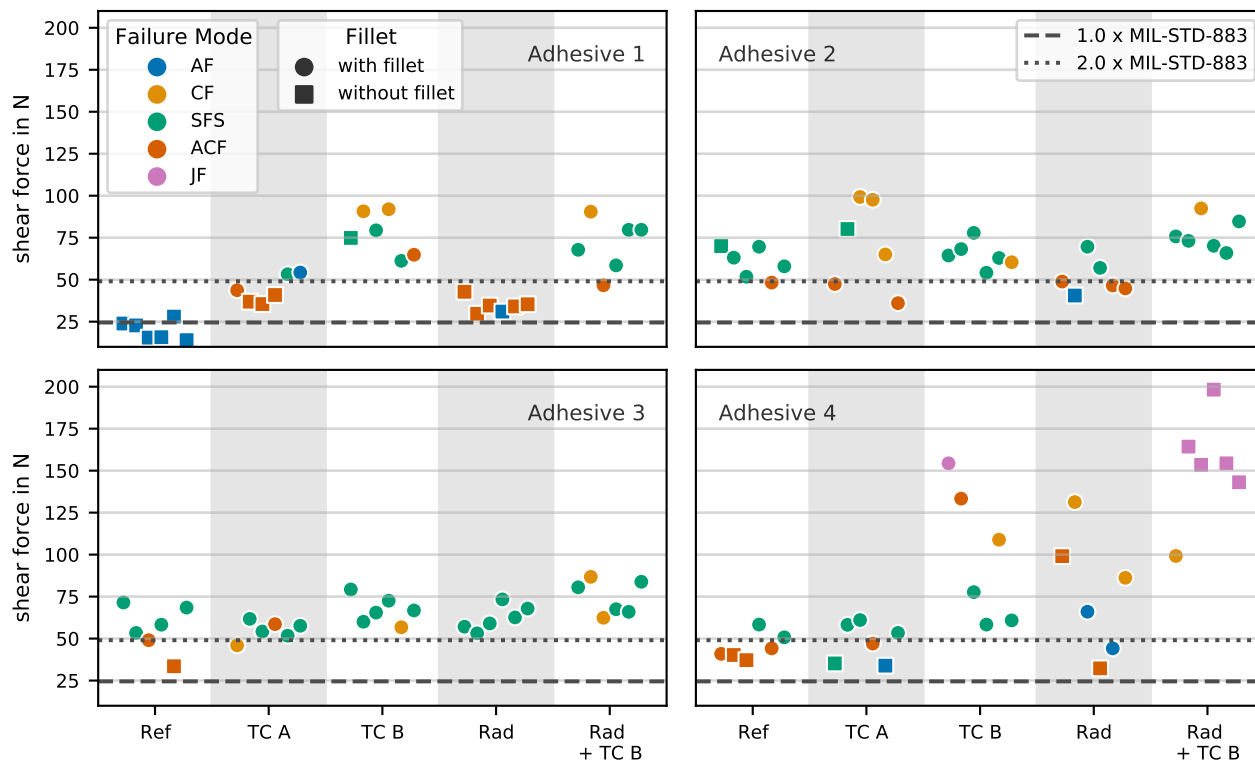


Figure 5. Failure mechanisms of the tested adhesive joints categorized according to the DIN EN ISO 10365 for the four adhesives and different environmental stresses according to Section 2.2. Additionally, the marker style indicates whether the sample had an adhesive fillet. If the image of a sample after shear testing shows a fillet on at least three sides, the bond is categorized as 'with fillet' and marked accordingly.

strength. Subsequent thermal stress according to TC B starts the polymer cross-linking again at the broken bonds and thus an increased bond strength is achieved.¹⁶

The results for **adhesive 3** in Fig. 3 exhibit the least variation of the bond strength with respect to the investigated thermal and radiative environmental loads. This hybrid curing adhesive passes the MIL-STD-883L Test Method 2019.9 requirement with factor 2x for each sample set and the variation of the sample mean for external stresses is within the error of each measurement. Furthermore, the variance for each stress is less compared to adhesive 1 and 2, which could be caused by reduced internal stress due to the additional heat curing. During the UV cure the polymer network forms rapidly, resulting in internal stresses within the network. Heating the sample can lead to a re-arrangement of the polymers when thermal part of the cure sets in, resulting in reduced stress and increased bond strength.

Adhesive 4 exhibits the highest bond strength values measured within this study, though standard deviation within each sample set is also very high (up to 39.78 N for TC B sample set). The bond strength of this hybrid curing adhesive increases when exposed to thermal or radiative stress compared to the reference set. The large scattering of the overall sample set for adhesive 4 can be explained by the more complex application procedure, cure schedule and shorter pot life for this adhesive. The shorter pot life probably also caused the sample set for Rad & TC B to not have fillets, since this set was set-up last and due to increased viscosity less adhesive is applied. Interestingly, the JF fracture mode still occurred basically only for this set. This shows a very strong interface between adhesive and glass block and an adhesive layer with high shear strength.

2.3 Influence of plasma cleaning on bond strength

One way to improve the bond strength of adhesive joints is plasma cleaning of the interface surfaces. Especially for joints that exhibit failures at the interface of adhesive and adherent (AF, ACF) plasma cleaning before

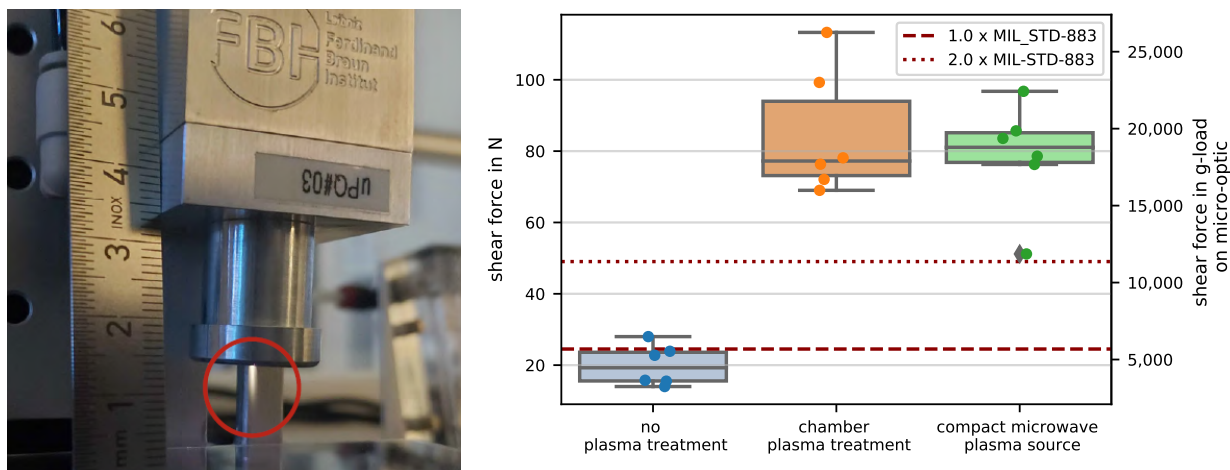


Figure 6. Left: the compact microwave plasma source (μ PQ), emitting a plasma jet at its nozzle (red circle). Right: influence of plasma surface cleaning on the shear strength of adhesive 1. A vacuum chamber plasma treatment and the compact microwave plasma source are investigated.

assembly is expected to increase the bond strength. A partially ionized gas, which in laboratory applications is usually generated by electric fields, is accelerated onto the surface that should be cleaned. Residual molecules on this surface are first physically ablated by this incident high-energy ions. For non-oxidizing materials often oxygen plasma is used, which then also chemically reacts with residual hydrocarbons on the surface. This process creates free bond sites on the surface, resulting in a better formation of chemical bonds with the epoxy polymer and hence increased bond strength.

The effect of two different plasma sources on the adhesive shear strength is investigated. The first source is a vacuum chamber plasma, where the samples are placed in a chamber and after pump-down treated with oxygen plasma for 30 s. This source has the advantage that it treats large surface areas or multiple samples at once and that the gaseous process products are directly pumped away. But since this is a rather large setup it is not available directly at the micro-integration facility. Therefore, the samples must be transported, which increases the time from surface cleaning/activation to assembly while the surface is exposed to air. This leads to an increasing occupation of the free bond sites on the surface, reducing the positive effects on the bond strength.

The second plasma source is the μ PQ (ultra-compact atmospheric pressure microwave plasma source, see Ref. 17), shown in Fig. 6. It is an in-house development of the FBH and generates a localized jet of atmospheric plasma (power 10 W to 20 W) and has a compact footprint ($114 \times 33 \times 25 \text{ mm}^3$). Here, gaseous process products are transported away by a constant stream of plasma and air from the source. In contrast to the chamber source, this compact device can be used directly at our micro-integration facility. Thus, the freshly cleaned and activated sample can be assembled directly after cleaning. The plasma is confined to a thin plasma jet, allowing a selective surface treatment, e.g., on substrates for optical assemblies as shown in Section 1. Our samples were cleaned for 6.5 s at 12 mm from the source.

For this study **adhesive 1** is used, since the sample set-up is best controlled. Also, this adhesive shows the lowest bond strength and also interface-related failure modes (AF, ACF) for the samples without fillet, compare to Section 2.2. Sample geometries, preparation and assembly is performed according to Section 2.1. As additional step plasma cleaning is performed after ultrasonic cleaning of the components. In addition to the reference set from Section 2.2, one sample set for each plasma cleaning method is assembled. To achieve comparable results, the samples were all prepared without fillet, which was confirmed by checking the microscope images after the die shear test. The results of the die shear strength test are compiled in Fig. 6. The reference set has a mean bond strength of 19.99 N and does not pass the MIL-STD-883L Test Method 2019.9 requirement of 24.5 N (factor 1.0x). After both plasma cleaning methods, the shear strength increases substantially and reaches a mean value of 84.68 N for the chamber plasma source and 78.67 N for the μ PQ source. All samples pass the MIL-STD-883L Test Method 2019.9 requirement of 49 N (factor 2.0x), even though there is one outlier for the μ PQ plasma

source.

In summary, the shear strength increased by a factor of approximately four compared to the reference set. Since all samples did not have fillets and interface failure modes occurred for the reference set this improvement is expected. The sample surfaces have fewer residual contaminations after the plasma cleaning and free bond sites at the interface surface allow for better chemical bonding of the polymer network. Both plasma cleaning methods increased the bond strength by a similar amount and the differences are within the margin of error. Further studies with an increased sample size, investigation of the effect for other failure modes, adhesives and environmental stresses need to be conducted in future.

3. SUMMARY AND OUTLOOK

Micro-integration of the optical systems for atom trapping and manipulation is one key method to realize compact, field and space compatible cold atom quantum sensors. Using this approach, an optical setup to generate a crossed beam optical dipole trap is assembled in a compact volume of ~ 25 mL, compare Section 1. As a next step we plan to combine such optical systems with atom chips within the UHV system of a cold atom quantum sensor, enabling hybrid trapping geometries in a compact and stable setup with low SWaP budget. Since our micro-optical systems rely on adhesive integration methods, these are qualified by die shear testing according to MIL-STD-883L Test Method 2019.9 in application relevant geometries, in our case for fused silica test bodies with a footprint of 2×4 mm². Samples are set-up for four adhesives with different curing mechanisms and environmentally aged by thermal cycling (up to -55 °C to 150 °C) and/or gamma-radiation ($10\,000$ mSv). Subsequent die shear testing shows for almost all sample sets a fulfillment of the MIL-STD-883L Test Method 2019.9 and a mostly increased bond strength for the environmentally aged samples. This can be explained by a better cross-linked polymer network and released stress of the adhesive layer after application of energy to the adhesive joint, see Section 2.2. Microscope images of the samples after testing are analyzed to evaluate failure mode and whether the joint has a fillet of adhesive. The weakest joints show a failure mode directly at the interface between adhesive layer and mostly the glass test body and a fillet increases the shear strength. For samples without fillets and exhibiting an interface failure mode the effect of two different plasma cleaning methods is investigated and shows an improvement by a factor of about four for the shear strength, compare Section 2.3. The shear strength tests showed overall a large variation, caused by the stronger influence of process parameters for small adhesive joints, e.g., interface properties, accuracy of alignment of test block and adhesive dispensing of small volumes. An increased sample size is necessary to reduce the variation.

In future, tensile strength tests of the adhesive joints are foreseen, which are expected to provide valuable information regarding the modulus of the joint. This, however, has proven difficult to accurately resolve for the thin layers of ≤ 30 μ m due to systematic errors of currently available testing setups and geometries. A new tensile strength test setup with dedicated measurement capabilities is planned. The investigated adhesives were selected, besides suitable mechanical, thermal and application properties, because they are promising regarding future application for UHV-compatible micro-optics assemblies. As next step we plan to qualify the adhesives, optical components, and the assembly procedure for UHV applications with an outgassing and mass spectrometry test bed, compare Ref. 11. For this, the accuracy of component mixing for two-component epoxies, the cross-linking of the polymer network and degree of cure is expected to be a significant variable. To further qualify these influences, parallel studies with calorimetry methods are foreseen, providing information about the glass transition temperature T_g of adhesives.

ACKNOWLEDGMENTS

We thank Robert Smol, Max Schiemangk and Andreas Wicht from the Joint Lab Quantum Photonic Components at FBH for their support and the provision of the micro-integration setup. We also thank Johannes Zender and Ulrike Winterwerber from the Prototype Engineering Lab at FBH for the provision of the μ PQ plasma source for this work.

This work is supported by the German Space Agency (DLR) with funds provided by the Federal Ministry for Economic Affairs and Climate Action (BMWK) due to an enactment of the German Bundestag under grant number 50WM1949 and 50RK1978.

REFERENCES

- [1] Oi, D. K. L., Ling, A., Grieve, J. A., Jennewein, T., Dinkelaker, A. N., and Krutzik, M., “Nanosatellites for quantum science and technology,” *Contemporary Physics* **58**(1), 25–52 (2017).
- [2] Grimm, R., Weidemüller, M., and Ovchinnikov, Y. B., “Optical Dipole Traps for Neutral Atoms,” *Advances In Atomic, Molecular, and Optical Physics* **42**, 95–170, Academic Press (2000).
- [3] Wicht, A., Bawamia, A., Krüger, M., Kürbis, C., Schiemangk, M., Smol, R., Peters, A., and Tränkle, G., “Narrow linewidth diode laser modules for quantum optical sensor applications in the field and in space,” **10085**, 100850F (2017).
- [4] Döringshoff, K., Gutsch, F. B., Schkolnik, V., Kürbis, C., Oswald, M., Pröbster, B., Kovalchuk, E. V., Bawamia, A., Smol, R., Schuldt, T., Lezius, M., Holzwarth, R., Wicht, A., Braxmaier, C., Krutzik, M., and Peters, A., “Iodine Frequency Reference on a Sounding Rocket,” *Physical Review Applied* **11**(5), 1 (2019).
- [5] Lezius, M., Wilken, T., Deutsch, C., Giunta, M., Mandel, O., Thaller, A., Schkolnik, V., Schiemangk, M., Dinkelaker, A., Kohfeldt, A., Wicht, A., Krutzik, M., Peters, A., Hellmig, O., Duncker, H., Sengstock, K., Windpassinger, P., Lampmann, K., Hülsing, T., Hänsch, T. W., and Holzwarth, R., “Space-borne frequency comb metrology,” *Optica* **3**(12), 1381 (2016).
- [6] Lachmann, M. D., Ahlers, H., Becker, D., Dinkelaker, A. N., Grosse, J., Hellmig, O., Müntinga, H., Schkolnik, V., Seidel, S. T., Wendrich, T., Wenzlawski, A., Carrick, B., Gaaloul, N., Lüdtke, D., Braxmaier, C., Ertmer, W., Krutzik, M., Lämmerzahl, C., Peters, A., Schleich, W. P., Sengstock, K., Wicht, A., Windpassinger, P., and Rasel, E. M., “Ultracold atom interferometry in space,” *Nature Communications* **12**(1), 1–6 (2021).
- [7] Becker, D., Lachmann, M. D., Seidel, S. T., Ahlers, H., Dinkelaker, A. N., Grosse, J., Hellmig, O., Müntinga, H., Schkolnik, V., Wendrich, T., Wenzlawski, A., Weps, B., Corgier, R., Franz, T., Gaaloul, N., Herr, W., Lüdtke, D., Popp, M., Amri, S., Duncker, H., Erbe, M., Kohfeldt, A., Kubelka-Lange, A., Braxmaier, C., Charron, E., Ertmer, W., Krutzik, M., Lämmerzahl, C., Peters, A., Schleich, W. P., Sengstock, K., Walser, R., Wicht, A., Windpassinger, P., and Rasel, E. M., “Space-borne Bose–Einstein condensation for precision interferometry,” *Nature* **562**(7727), 391–395 (2018).
- [8] Frye, K., Abend, S., Bartosch, W., Bawamia, A., Becker, D., Blume, H., Braxmaier, C., Chiow, S.-W., Efremov, M. A., Ertmer, W., Fierlinger, P., Franz, T., Gaaloul, N., Grosse, J., Grzeschik, C., Hellmig, O., Henderson, V. A., Herr, W., Israelsson, U., Kohel, J., Krutzik, M., Kürbis, C., Lämmerzahl, C., List, M., Lüdtke, D., Lundblad, N., Marburger, J. P., Meister, M., Mihm, M., Müller, H., Müntinga, H., Nepal, A. M., Oberschulte, T., Papakonstantinou, A., Perovsek, J., Peters, A., Prat, A., Rasel, E. M., Roura, A., Sbroscia, M., Schleich, W. P., Schubert, C., Seidel, S. T., Sommer, J., Spindeldreier, C., Stamper-Kurn, D., Stuhl, B. K., Warner, M., Wendrich, T., Wenzlawski, A., Wicht, A., Windpassinger, P., Yu, N., and Wörner, L., “The Bose-Einstein Condensate and Cold Atom Laboratory,” *EPJ Quantum Technology* **8**(1), 1 (2021).
- [9] Keil, M., Amit, O., Zhou, S., Groswasser, D., Japha, Y., and Folman, R., “Fifteen years of cold matter on the atom chip: promise, realizations, and prospects,” *Journal of Modern Optics* **63**(18), 1840–1885 (2016).
- [10] Kassner, A., Rechel, M., Heine, H., Herr, W., Christ, M., Krutzik, M., Rasel, E. M., and Wurz, M. C., “Atom Chip technology for use under UHV conditions,” *Smart Systems Integration; 13th International Conference and Exhibition on Integration Issues of Miniaturized Systems, Barcelona, Spain*, 69–75 (2019).
- [11] Christ, M., Kassner, A., Smol, R., Bawamia, A., Heine, H., Herr, W., Peters, A., Wurz, M. C., Rasel, E. M., Wicht, A., and Krutzik, M., “Integrated atomic quantum technologies in demanding environments: development and qualification of miniaturized optical setups and integration technologies for UHV and space operation,” *CEAS Space Journal* **11**(4), 561–566 (2019).
- [12] Habenicht, G., [*Kleben*], Springer Berlin Heidelberg, Berlin, Heidelberg (2009).
- [13] Adams, R. D. and Peppiatt, N. A., “Stress analysis of adhesive-bonded lap joints,” *Journal of Strain Analysis* **9**(3), 185–196 (1974).
- [14] da Silva, L. F. M., “Design Rules and Methods to Improve Joint Strength,” in [*Handbook of Adhesion Technology*], 689–723, Springer Berlin Heidelberg, Berlin, Heidelberg (2011).
- [15] Habenicht, G., [*Kleben - erfolgreich und fehlerfrei*], Springer Fachmedien Wiesbaden, Wiesbaden (2016).

- [16] Al-Attabi, A., Fouracre, R. A., Banford, H. M., and Tedford, D. J., “High dose neutron and gamma-radiation effects in an epoxy resin,” *International Journal of Radiation Applications and Instrumentation. Part 40*(5), 411–419 (1992).
- [17] Wolf, D., “Resonator und Leistungoszillator zum Aufbau einer integrierten Plasmaquelle sowie deren Verwendung,” *Patent*, DE 10 2020 100 872 B4 2021.08.05 (2021).